PARTICLE ENTRAINMENT MECHANISMS BY SMALL-SCALE TURBULENT VORTEX VIA DIRECT NUMERICAL SIMULATIONS

Rajesh Ramesh
School for Engineering of Matter, Transport and Energy
Arizona State University
Tempe, Arizona, USA
rrames34@asu.edu

Yulia Peet
School for Engineering of Matter, Transport and Energy
Arizona State University
Tempe, Arizona, USA
ypeet@asu.edu

ABSTRACT

We investigate particle–vortex interactions in a model tornado-like flow setup using a four-way coupled Euler–Lagrange framework. Simulations are performed at two swirl ratios, S=1.25 and S=2.16, while keeping aspect ratio and radial Reynolds number fixed. Simulations begin in the absence of particles by solving the unfiltered Navier-Stokes equations. Results are then presented in the form of velocity flow fields that are azimuthally averaged. The velocity flow fields show the prominent features of a tornado-like vortex, including the presence of a vortex core with a strong swirl, and an updraft outside the core. Once the tornado-like flow is established, a uniform cloud of particles is introduced, subsequently evolving with the flow. At both swirl ratios, the particle cloud undergoes radial compression and vertical extension, accompanied by particle clustering at its sides. At a later time, particles start to escape from the bulk of the cloud and gain higher velocities. The rate at which particles escape is compared for both swirl ratios, showing higher escape rates at a higher swirl ratio. Finally, the hydrodynamic forces on the particles are shown to be dominated by drag, with shear-induced lift playing a secondary role.

INTRODUCTION

Tornado-like vortices represent a class of swirling flows characterized by strong rotation, radial inflow, and vertical updraft (Refan & Hangan, 2016; Ward, 1972). Canonical analytical models, such as the Burgers vortex and the Sullivan vortex, capture key features of such flows, including a viscous core with a tangential velocity profile similar to the Lamb–Oseen vortex (Panton, 2013). In these models, radial inflow balances viscous diffusion, sustaining the vortex structure. While analytical solutions exist at low Reynolds numbers, higher Reynolds number flows—particularly in the presence of a ground boundary—exhibit significantly more complex behavior.

One of the most prominent features in such regimes is vortex breakdown, where the initially coherent vortex core becomes unstable and undergoes structural changes along the vertical direction. As the swirl ratio increases, the location of vortex breakdown shifts downward, and at sufficiently high swirl, breakdown can occur near the surface, leading to the formation of multiple vortical structures (Refan & Hangan, 2016). These dynamics are directly relevant to geophysical flows such as tornadoes and dust devils, which operate at high Reynolds numbers and are capable of entraining and transporting large quantities of particulate matter, including dust, sand, and debris.

Understanding the behavior of particles within such vortical flows is of both scientific and practical importance. The transport of inertial particles in tornado-like vortices is governed by a complex interplay between fluid-induced forces (e.g., drag, lift, and pressure gradients), gravitational settling, and particle inertia. These effects are often characterized by non-dimensional parameters such as the Stokes number and Galileo number, in addition to flow parameters like Reynolds number, swirl ratio, and aspect ratio.

At sufficiently high mass loadings, particle–fluid interactions become strongly coupled. In such regimes, not only do particles respond to the flow, but they also modify it through interphase momentum exchange. Furthermore, effects such as preferential concentration, turbhophoresis, gravitational settling can lead to high local volume fractions making volume effects and particle-particle collisions important. These phenomena necessitate modeling approaches that account for both momentum coupling, volume exclusion effects, and particle-particle collisions. Volume-filtered formulations of the Navier–Stokes equations provide a suitable framework for capturing these interactions (Jackson & Anderson, 1967), as described in the following section.

While particle-laden flows have been extensively studied in canonical configurations such as homogeneous isotropic turbulence and turbulent channel flow, relatively fewer studies have examined particle dynamics in vortex-dominated flows (Mehrabadi *et al.*, 2018; Wang *et al.*, 2019; Costa *et al.*, 2020). Recent work has explored particle dispersion in simplified vortex configurations, such as a quasi-two-dimensional Lamb–Oseen vortex (Shuai & Kasbaoui, 2022). However, the behavior of particles in fully three-dimensional, tornado-like vortices–particularly in the presence of strong coupling and gravitational effects–remains less well understood.

In this study, we investigate particle–vortex interactions in a tornado-like flow, with a focus on the role of swirl ratio in governing particle transport, clustering, and escape dynamics. By performing high-fidelity simulations using a four-way coupled Euler–Lagrange framework, we aim to quantify how particles modify the flow field and, in turn, how vortex dynamics influence particle behavior.

METHODOLOGY

We use the four-way coupled Euler-Lagrange (EL) methodology to model this multiphase flow problem. The EL methodology treats the fluid (carrier phase) as a continuous phase while the dispersed phase (particles) is treated as a discrete phase by tracking each particle individually (Balachandar & Eaton, 2010). This model assumes that particles are smaller than the Kolmogorov length scale of the flow ($d_p \lesssim \eta$) to satisfy the point-particle assumption. The governing equations for this multiphase flow system are derived by volume filtering the single-phase Navier-Stokes equations (Zwick & Balachandar, 2020),

$$\nabla \cdot \mathbf{u} = -\frac{1}{\phi_f}\frac{D\phi_f}{Dt}, \tag{1}$$

$$\frac{D\mathbf{u}}{Dt} = -\frac{\nabla p}{\rho_f} + \nu_f \nabla \cdot \left(\nabla \mathbf{u} + \nabla \mathbf{u}^T\right) + \frac{\mathbf{f}_{\mathrm{pf}}}{\rho_f \phi_f}, \tag{2}$$

where $\mathbf{u}$, p, ν_f, ρ_f and ϕ_f are, respectively, the fluid velocity, pressure, kinematic viscosity, density, and fluid volume fraction. The $\mathbf{f}_{pf}$ is the coupling force from the particles on the fluid. The fluid volume fraction is calculated based on the particle volume fraction as

$$\phi_f = 1 - \phi_p \tag{3}$$

The particle volume fraction and the coupling force from the particles are obtained by projecting the particle quantities, i.e. the particle volume and the particle-fluid coupling forces, respectively, onto the Eulerian frame. The projection operation uses an isotropic Gaussian kernel, $g_M(r)$, with a filter width, $\delta_f = 5d_p$, and is defined as

$$g_M(r) = \frac{1}{\sigma(\sqrt{2\pi})^3}\exp\left(-\frac{r^2}{2\sigma^2}\right) \tag{4}$$

where $\sigma = \delta_f/(2\sqrt{2\ln(2)})$. With this kernel, the particle volume fraction is defined as

$$\phi_p = \sum_{i=1}^{N_p} V_{p,i} g_M(|x - X_i|) \tag{5}$$

where $V_{p,i}$ is the volume of the i^{th} particle, and the particle coupling force is defined as

$$\mathbf{f}_{pf} = \sum_{i=1}^{N_p} \mathbf{F}_{pf,i} g_M(|x - X_i|) \tag{6}$$

where $\mathbf{F}_{pf,i} = \mathbf{F}_{drag,i} + \mathbf{F}_{lift,i}$, with $\mathbf{F}_{drag,i}$ and $\mathbf{F}_{lift,i}$ representing the drag and lift forces on the i^{th} particle, respectively.

We also define the volume filtered particle velocity in the Eulerian frame, given by

$$\phi_p \mathbf{u}_p = \sum_{i=1}^{N_p} V_{p,i} \mathbf{V}_i\, g_M(|\mathbf{x} - \mathbf{X}_i|), \tag{7}$$

where $\mathbf{V}_i$ denotes the i^{th} particle velocity, used for analysis and visualization of particle velocity fields.

The particles, on the other hand, are solved in a Lagrangian reference frame, with the equations of motion

$$\frac{d\mathbf{X}}{dt} = \mathbf{V}, \tag{8}$$

$$\rho_p \frac{\pi}{6} d_p^3 \frac{d\mathbf{V}}{dt} = \mathbf{F}_g + \mathbf{F}_{drag} + \mathbf{F}_{lift} + \mathbf{F}_{pg} + \mathbf{F}_{col}, \tag{9}$$

$$I\frac{d\Omega}{dt} = \mathbf{M}_F + \mathbf{M}_C + \mathbf{M}_R. \tag{10}$$

Here, $\mathbf{X}$, $\mathbf{V}$, d_p, and ρ_p represent coordinates, velocities, diameter and density of the particles, and $\mathbf{F}_g$, $\mathbf{F}_{drag}$, $\mathbf{F}_{lift}$, $\mathbf{F}_{pg}$, $\mathbf{F}_{col}$ correspond to the gravitational, drag, lift, pressure gradient and collision forces on a particle, respectively. I is the particle's moment of inertia defined by $I = \rho_p(\pi/60)d_p^5$, Ω is the particle's angular velocity and the terms $\mathbf{M}_F$, $\mathbf{M}_C$ and $\mathbf{M}_R$ corresponds to the hydrodynamic torque, collision torque and the rolling resistance, respectively. The drag force is modeled with Gidaspow drag correlation (Gidaspow, 1994), lift consists of both Saffman (Saffman, 1965) and Magnus (Magnus, 1852) forces, and the collision forces are represented by a soft-sphere collision model (Cundall & Strack, 1979).

The Saffman lift force is a shear-induced lift force modeled using the local flow vorticity,

$$\mathbf{F}_{saffman} = 1.615\rho_f \nu_f d_p |\mathbf{V}_\mathbf{s}| \sqrt{\frac{d_p^2|\omega|}{\nu_f}}\frac{\omega \times \mathbf{V}_s}{|\omega||\mathbf{V}_s|}, \tag{11}$$

where ω is the flow vorticity and $\mathbf{V}_s$ is the slip velocity given by $\mathbf{V}_s = \mathbf{V} - \mathbf{u}_{|\mathbf{x}=\mathbf{X}}$. The Magnus lift force accounts for the lift generated by the particle's rotation and is defined as

$$\mathbf{F}_{magnus} = \frac{\pi}{8} d_p^3 (\omega - \Omega) \times \mathbf{V}_s. \tag{12}$$

The collisional forces are handled through a soft-sphere spring damper collision model originally proposed by Cundall and Strack (1979). The collisional force has a normal component which acts along the direction of the normal vector, $\mathbf{n}_{ij}$, from the center of i^{th} particle to the center of j^{th} particle,

$$\mathbf{F}_{c,\mathrm{normal}} = \sum_{j=1}^{N_p} -k_c\, \delta_{ij}\mathbf{n}_{ij} - \eta_n \mathbf{V}_{ij,n}, \tag{13}$$

where k_c is the spring constant, δ_{ij} is the overlap between the particles, η_n is the normal damping coefficient, and $\mathbf{V}_{ij,n}$ is the normal relative contact velocity. The damping coefficient is given by

$$\eta_n = -2\sqrt{M_{ij}k_c} \cdot \frac{\ln e_n}{\sqrt{(\ln e_n)^2 + \pi^2}}, \quad M_{ij} = \left(\frac{1}{M_i} + \frac{1}{M_j}\right)^{-1}, \tag{14}$$

where M_{ij} is the effective mass and e_n is the coefficient of restitution.

The collisional force also has a tangential component which uses a Coloumb friction model assuming the particles maintain a slipping contact. A viscous friction which is proportional to the relative velocity is also introduced to prevent unphysical oscillations at low slip-rates,

$$\mathbf{F}_{c,\text{tangential}} = -\min\{\mu_{\text{friction}}|\mathbf{F}_{c,\text{normal}}|, \eta_t|\mathbf{V}_{ij,t}|\}\mathbf{t}_{ab}, \tag{15}$$

where $\mathbf{t}_{ab}$ is the unit vector parallel to the relative tangential velocity given by $\mathbf{V}_{ij,t}$, μ_{friction} is the Coulomb friction coefficient, and η_t is the tangential damping coefficient, which we set as $\eta_t = \eta_n$ in this study.

In the soft-sphere collision model, the stiffness coefficient k_c is selected to limit the maximum particle overlap to below 5% of the particle diameter and a restitution coefficient e_n of 0.9, ensuring realistic collision behavior (Capecelatro & Desjardins, 2013). The collision timescale is given by $t_c = \sqrt{M_{ij}(\ln(e_n)^2 + \pi^2)/k_c}$. Therefore, the time step Δt used in the simulations is chosen to adequately resolve the particle collision timescale t_c such that $\Delta t = t_c/30$. This collision timescale constraint is the limiting factor for the time step selection, as the flow time step imposed by the CFL condition is significantly larger.

The EL methodology is implemented in a Fortran library known as ppiclF (Zwick & Balachandar, 2020). The library is used with Nek5000, a spectral element method code that solves incompressible fluid flow equations. A point-particle Direct Numerical Simulation (DNS) approach resolving eddies of the flow that are larger than the filter width, combined with a stabilizing spectral filter (Mullen & Fischer, 1999), is employed in this study.

SIMULATION SETUP

The simulation setup consists of a cylinder of radius R divided into 2 sections by a horizontal plane at height h as shown in Figure 1, resembling a setup of our prior study (Kang *et al.*, 2025) that focused on vortex flow analysis without particles. The bottom section has a velocity inlet condition at the lateral surface of the cylinder and the no-slip wall condition at the bottom surface, while the top section has a slip wall condition at the lateral surface and an outlet condition at the top surface. We specify both tangential and radial velocity component at the inlet as shown in Figure 1a.

The cylinder geometry is meshed using the O-grid technique with structured hexahedral elements. The mesh consists of 43,890 elements, each with 8^3 Gauss-Lobatto-Legendre grid points. The ratio of the filter width to the element length (δ_f/L_e) is maintained above 0.75 ensuring that the filter is numerically resolved everywhere.

Previous laboratory and numerical studies (Refan & Hangan, 2016; Lewellen *et al.*, 2000; Church *et al.*, 1979; Ward, 1972) have shown that the radial Reynolds number

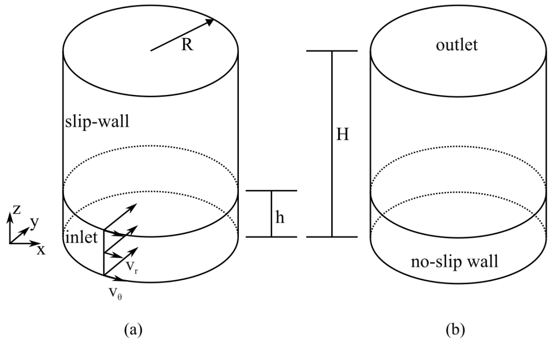

Figure 1. Schematic of the simulation domain with boundary conditions. (a) shows velocity inlet ($v_r = U_{inlet}$, $v_\theta = U_{inlet}tan(\theta)$) at the lateral boundary below $z = h$, and slip wall above $z = h$; (b) shows no-slip wall at the bottom, outlet at the top.

($Re_r = (2U_{inlet}R)/\nu_f$), aspect ratio ($a = h/R$, where h is the inlet height and R is the updraft radius) and the swirl ratio ($S = tan(\theta)/(2a)$) are the major non-dimensional parameters that set the dynamics of the tornado-like vortex flow. In this work, we vary the swirl ratio while keeping the other parameters constant: i) $S = 1.25$, and ii) $S = 2.16$, both at $a = 0.4$ and $Re_r = 625$. In particular, we keep a radial inlet velocity $v_r = U_{inlet}$ constant across the cases, while different swirl ratios are established by varying the injection angle θ and, consequently, the inlet tangential velocity. Simulations were first performed without particles. At the beginning of this simulation, the fluid velocity is zero everywhere. After the simulation runs for a time of $t/T = 20$, where $T = (2R)/U_{inlet}$, the vortex flow develops and reaches a state where the mean flow statistics become stationary with time. The developed single-phase vortex flow is used as an initial condition for the simulations where particles are introduced to the flow.

Particles with diameter, $d_p/(2R) = 0.005$, and density ratio, $\rho_p/\rho_f = 2000$, are initially introduced into the near-wall layer just above the ground. Particles are arranged regularly in a cylindrical grid-like pattern with an inter-particle distance of $2d_p$ in radial, vertical, and azimuthal directions. The pattern consists of 25 layers that reach a height of about $1.2h$ starting from the ground, with each layer covering the entire horizontal cross-section of the cylinder. A total number of particles across all the layers is $N_0 = 192,450$. The initial average volume fraction within this particle cloud is $\phi_{p0} = 0.065$. The initial velocities of all the particles are zero. The simulations with particles are run from this initial condition and until the time of $t/T = 1.65$. The Galileo number defined by $Ga = \sqrt{(\rho_p/\rho_f - 1)\, g\, d_p^3}/\nu_f$ is 3.9 which ensures that bulk of the particles remain in a suspended state balancing the gravitational force balanced and the upward drag force for the given Reynolds number of the flow. The Stokes number is defined by $St \equiv \tau_p/\tau_f$, where $\tau_p = (\rho_p d_p^2)/(18\mu_f)$ is the particle response time, and τ_f is the characteristic time driving the particle motion. Assuming $\tau_\eta \lesssim \tau_f \lesssim T$, where τ_η is the Kolmogorov time scale, Stokes number lies in the range $St = O(1) - O(10^2)$.

RESULTS

In Figure 2, we show the fluid flow velocity field for the tornado-like vortex in the absence of particles for S=1.25 and

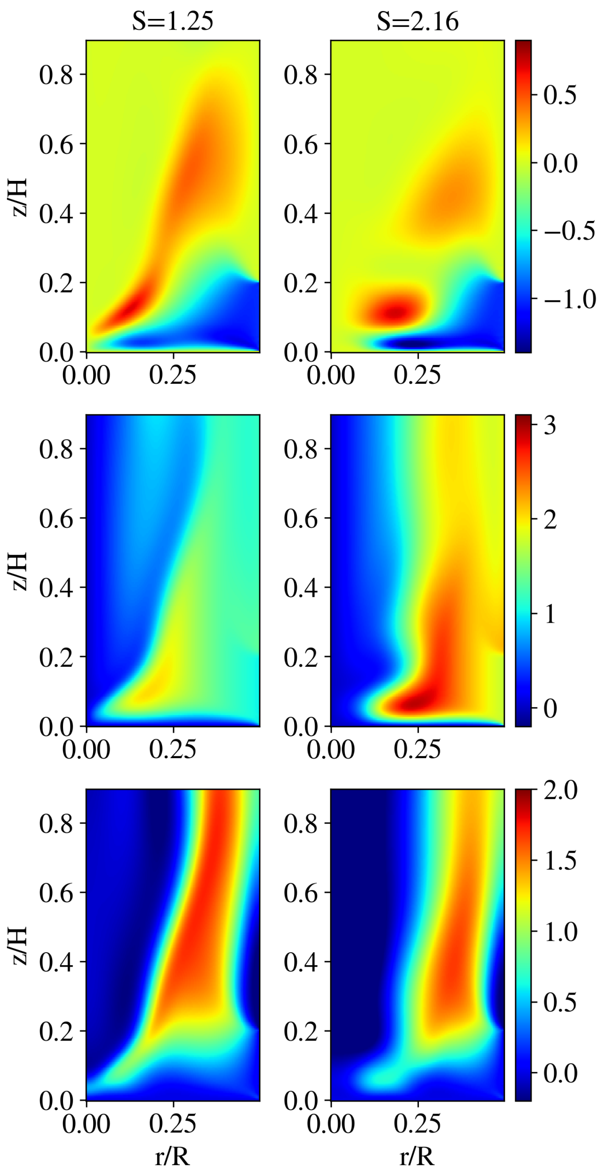

Figure 2. Azimuthally averaged normalized flow velocity components for radial velocity, v_r/U_{inlet} (top), azimuthal velocity, v_θ/U_{inlet} (middle), and vertical velocity, v_z/U_{inlet} (bottom), in the absence of particles for *S*=1.25 and *S*=2.16.

S=2.16. The vortex flow structure has a central core region where the mean velocity magnitude is low compared to velocity magnitude outside the core. The flow originating from the inlet radially converges towards the core and is subsequently advected upward without penetrating the core. The strong updraft is characterized by a high upward flow velocity and the strong swirl is characterized by the high tangential flow velocity. As expected, the swirl is stronger for the flow with the higher swirl ratio. For both cases, the vortex core starts out to be narrow at the surface and broadens with height; however, the vortex core starts out wider for *S*=2.16.

Next, we examine how the particle cloud interacts with and modifies the tornado flow structure. As the simulation progresses, the initial particle cloud changes in shape as it interacts with the vortex flow. In Figure 3, we show the particle volume fraction at four different simulation times. The cloud of particles is progressively compressed from the sides while it forms a rim at the top. As it does so, particles start clustering

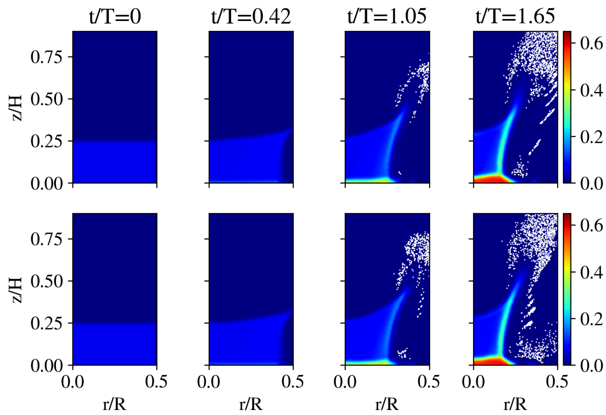

Figure 3. Azimuthally averaged particle volume fraction for *S*=1.25 (top) and *S*=2.16 (bottom) at four different simulation times: $t/T = 0$, $t/T = 0.42$, $t/T = 1.05$, $t/T = 1.65$ (from left to right).

at the periphery of the cloud, as observed in the particle volume fraction field at later times, consistent with preferential concentration mechanisms for particles with Stokes number of order unity (Fessler *et al.*, 1994). Additional clustering is observed near the ground where the particles densely accumulate. At later times, particles start to escape from the sides of the domain. The particles that tend to escape are dispersed at a very low volume fraction compared to the bulk volume fraction of the cloud. Therefore, to visualize them, we use a much lower threshold of volume fraction ($\phi_p < 0.004$) to detect these particles individually and mark their $r-z$ coordinates with white dots on top of the volume fraction field. We can see that these escaped particles come from the sides and the rim of the cloud.

Further insights indicate that the overall shape of the particle cloud is primarily governed by the radial inflow rather than the swirl ratio. In both cases, irrespective of the swirl ratio, the inward radial motion governed by the radial component of the inlet velocity, which is the same for both swirl ratios, leads to a similar large-scale compression of the cloud. However, higher swirl seems to promote increased particle ejection from the sides of the cloud. Nevertheless, the difference in particle ejection rate remains modest, and its influence on the overall shape of the particle cloud as a function of swirl ratio is limited (Figure 3).

In Figure 4, we show the azimuthally averaged fluid flow velocity field in the presence of particles at $t/T = 1.65$ for *S*=1.25 and *S*=2.16. Although the flow is evolving, the presence of particles leads to velocity fields that differ markedly from the particle-free case. Unlike in Figure 2, the vortex core now has a similar shape in both swirl ratios. The vortex core starts out much wider near the surface as it broadens with height. Therefore, we can see that the particle cloud has altered the initial structure of the vortex core. However, the swirl still remains stronger for the flow with the higher swirl ratio.

In Figure 5, we show the azimuthally averaged particle velocity field projected onto the Eulerian frame at $t/T = 1.65$. The velocity field indicates that particles within the core of the vortex, where the bulk of the cloud resides, move very slowly whereas the escaped particles have much higher velocities. However, the particles generally move 2–3 times slower than the fluid; this sluggish behavior is a result of the high Stokes number. The radial particle velocity field shows these escaped particles being ejected radially outwards while the tangential

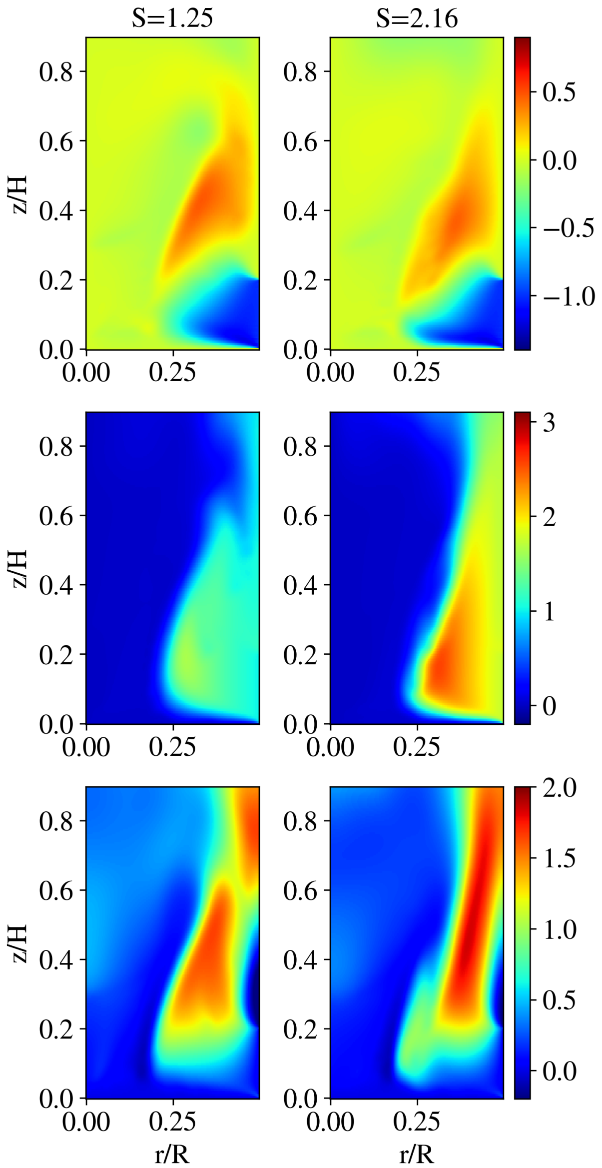

Figure 4. Azimuthally averaged normalized flow velocity components for radial velocity, v_r/U_{inlet} (top), azimuthal velocity, v_θ/U_{inlet} (middle), and vertical velocity, v_z/U_{inlet} (bottom), in the presence of particles for S=1.25 and S=2.16 at $t/T = 1.65$.

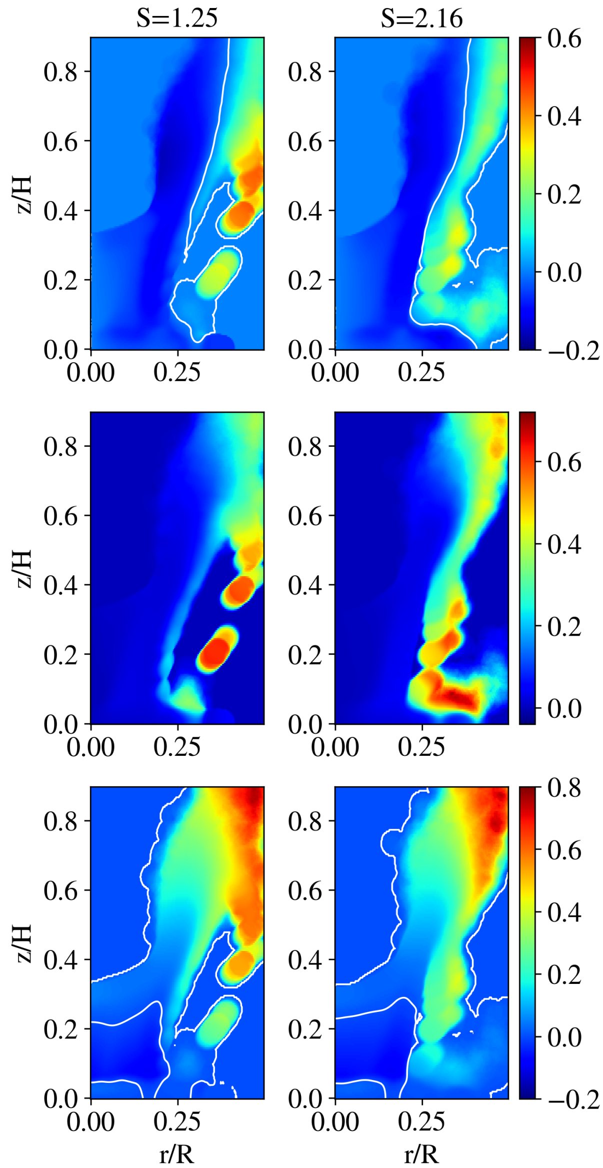

Figure 5. Azimuthally averaged Eulerian particle velocity components for radial velocity, $u_{p,r}/U_{inlet}$ (top), azimuthal velocity, $u_{p,\theta}/U_{inlet}$ (middle), and vertical velocity, $u_{p,z}/U_{inlet}$ (bottom) for S=1.25 and S=2.16 at $t/T = 1.65$. White line denotes zero-velocity isocontour.

particle velocity field shows that the particles co-rotate with the flow, albeit at a lower angular velocity. The vertical particle velocity field shows a fraction of the escaped particles entrained in the updraft and exit the domain through the top.

To quantify the rate at which particles escape, we calculate the number of particles in the domain as a function of time. The number of particles in the domain, shown in Figure 6, initially decreases at the same rate for both swirl ratios, while a decrease becomes more substantial for the higher swirl ratio at a non-dimensional time $t/(2R/U_{inlet}) \sim 0.6$. The loss of particles in the domain is associated with the particles' escape through the lateral and top domain boundaries as they cannot escape through the bottom surface. This particle escape occurs more rapidly at higher swirl ($S = 2.16$), which can be attributed to stronger centrifugal effects that enhance radial ejection of particles.

To understand the governing mechanisms of particle

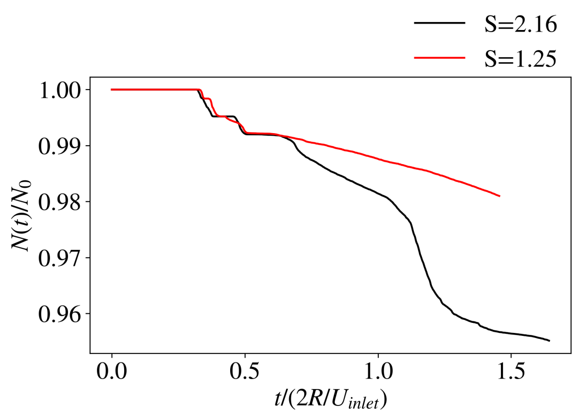

Figure 6. Temporal evolution of the fraction of particles in the domain for $S = 1.25$ and $S = 2.16$.

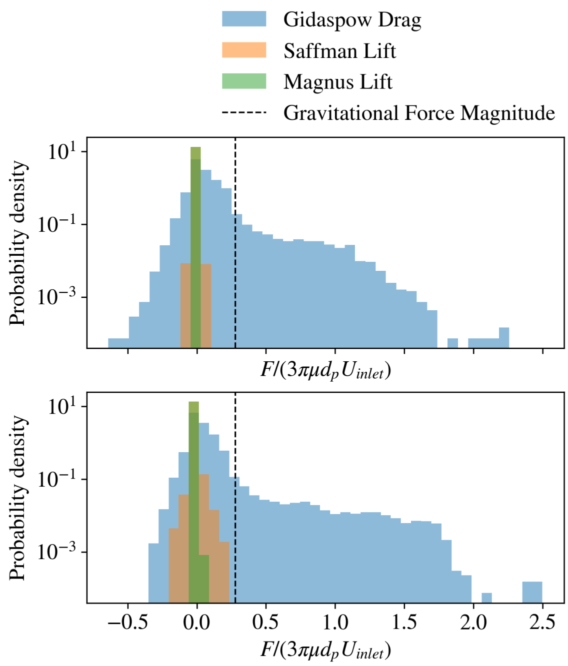

Figure 7. Probability density of the vertical component of fluid-induced forces (drag, lift) compared with the magnitude of the gravitational force on the particles for S=1.25 (top) and S=2.16 (bottom) at $t/T = 1.65$.

transport, we examine the relative importance of hydrodynamic forces acting on the particles. In Figure 7, we show the probability density distribution of the hydrodynamic force components acting on the particles in the vertical direction at $t/T = 1.65$. For both cases, hydrodynamic force on the particles is dominated by the fluid drag force. The Saffman and Magnus components of the lift force remain below the gravitational force in both cases. While lift due to rotation (Magnus lift) stays close to zero at both swirl ratios, lift due to shear (Saffman lift) increases as swirl ratio increases, showing a higher importance of shear-dominated effects at high swirl ratios.

CONCLUSIONS

In this work, we investigated particle–vortex interactions in a model tornado-like vortex flow using a four-way coupled Euler–Lagrange simulation framework, with a focus on the effect of the swirl ratio. The particles considered in this study are highly inertial with the gravitational effect included.

The evolution of the particle cloud is primarily governed by radial inflow, which drives its compression and determines its overall structure. Particle clustering is observed at the cloud periphery and near the ground which is possibly due to preferential concentration and gravitational effects. A small fraction of particles escape from the lateral sides and the rim of the particle cloud which ultimately leave the flow domain. The number of particles that leave the domain increases with swirl ratio for the same time window. Therefore, increasing the swirl ratio does seem to increase the particle escape rate.

The presence of a dense particle cloud significantly modifies the flow field, including the size of the vortex core. In the absence of particles, vortex core size is dependent on the swirl ratio of the flow. However, when particles are introduced, the vortex core size remains unaffected by the swirl ratio. Finally, the shear induced-lift forces are shown to have a secondary effect on the particle dynamics while drag force still remains as the dominant hydrodynamic force.

REFERENCES

Balachandar, S. & Eaton, J. K. 2010 Turbulent dispersed multiphase flow. *Annu. Rev. Fluid Mech.* **42** (1), 111–133.

Capecelatro, J. & Desjardins, O. 2013 An Euler–Lagrange strategy for simulating particle-laden flows. *Journal of Computational Physics* **238**, 1–31.

Church, C. R., Snow, J. T., Baker, G. L. & Agee, E. M. 1979 Characteristics of tornado-like vortices as a function of swirl ratio: A laboratory investigation. *Journal of Atmospheric Sciences* **36** (9), 1755–1776.

Costa, P., Brandt, L. & Picano, F. 2020 Interface-resolved simulations of small inertial particles in turbulent channel flow. *Journal of Fluid Mechanics* **883**, A54.

Cundall, P. A. & Strack, O. D. L. 1979 A discrete numerical model for granular assemblies. *Geotechnique* **29** (1), 47–65.

Fessler, J. R., Kulick, J. D. & Eaton, J. K. 1994 Preferential concentration of heavy particles in a turbulent channel flow. *Physics of Fluids* **6** (11), 3742–3749.

Gidaspow, D. 1994 *Multiphase flow and fluidization: continuum and kinetic theory descriptions*. Academic Press.

Jackson, R. T. & Anderson, R 1967 A fluid mechanical description of fluidized beds. *Industrial & Engineering ACS-Chemistry Fundamentals* **6** (4), 527–539.

Kang, S., Ramesh, R., Peet, Y. & Chamorro, L. P. 2025 Influence of swirl ratio on the structure and dynamics of tornado-like vortices. *Physics of Fluids* **37** (5), 057135.

Lewellen, D. C., Lewellen, W. S. & Xia, J. 2000 The influence of a local swirl ratio on tornado intensification near the surface. *Journal of the Atmospheric Sciences* **57** (4), 527–544.

Magnus, G. 1852 *Ueber die Abweichung der Geschosse nebst einem Anhange: Ueber eine auffallende Erscheinung bei rotirenden Körpern*. Dümmler.

Mehrabadi, M., Horwitz, J. A. K., Subramaniam, S. & Mani, A. 2018 A direct comparison of particle-resolved and point-particle methods in decaying turbulence. *Journal of Fluid Mechanics* **850**, 336–369.

Mullen, J. S. & Fischer, P. F. 1999 Filtering techniques for complex geometry fluid flows. *Communications in Numerical Methods in Engineering* **15** (1), 9–18.

Panton, R. L. 2013 *Some Solutions of the Navier–Stokes Equations*, chap. 11, pp. 220–265. John Wiley Sons, Ltd.

Refan, M. & Hangan, H. 2016 Characterization of tornado-like flow fields in a new model scale wind testing chamber. *J. Wind Eng. Ind. Aerodyn* **151**, 107–121.

Saffman, P. G. 1965 The lift on a small sphere in a slow shear flow. *Journal of Fluid Mechanics* **22** (2), 385–400.

Shuai, S. & Kasbaoui, M. H. 2022 Accelerated decay of a Lamb–Oseen vortex tube laden with inertial particles in Eulerian–Lagrangian simulations. *Journal of Fluid Mechanics* **936**, A8.

Wang, G., Fong, K. O., Coletti, F., Capecelatro, J. & Richter, D. H. 2019 Inertial particle velocity and distribution in vertical turbulent channel flow: A numerical and experimental comparison. *Int. J. Multiphase Flow* **120**, 103105.

Ward, Neil B 1972 The exploration of certain features of tornado dynamics using a laboratory model. *Journal of Atmospheric Sciences* **29** (6), 1194–1204.

Zwick, D. & Balachandar, S. 2020 A scalable Euler–Lagrange approach for multiphase flow simulation on spectral elements. *Int. J. High Perf. Comp. Appl.* **34** (3), 316–339.